## Optical Engineering

Optical Engineering. SPIED igital Library.org

# Visualization of all-sky polarization images referenced in the instrument, scattering, and solar principal planes

Laura M. Eshelman Joseph A. Shaw



Laura M. Eshelman, Joseph A. Shaw, "Visualization of all-sky polarization images referenced in the instrument, scattering, and solar principal planes," *Opt. Eng.* **58**(8), 082418 (2019), doi: 10.1117/1.OE.58.8.082418.

### Visualization of all-sky polarization images referenced in the instrument, scattering, and solar principal planes

Laura M. Eshelman and Joseph A. Shaw\*

Montana State University, Department of Electrical and Computer Engineering, Bozeman, Montana, United States

**Abstract.** Sunlight becomes partially linearly polarized when scattered from atmospheric gas molecules and can be quantified using the linear Stokes parameters  $S_0$ ,  $S_1$ ,  $S_2$  and the derived degree of linear polarization and angle of polarization (AoP). The angle-dependent Stokes parameters  $S_1$  and  $S_2$  and the AoP require a reference plane. Commonly used reference planes for polarimetric applications include the instrument, scattering, and solar principal planes, each of which provides unique insights when analyzing sky polarization data. Methods to transform the parameters between each frame of reference are known; however, previous publications have not shown the results of transforming a time series of all-sky polarization images into these different reference planes clearly showing how this alters the image visualization. We review two methods used to rotate all-sky polarization images from the instrument to the scattering plane and the solar principal plane, and for the first time shows all-sky polarization image sequences recorded from sunrise to sunset of Stokes  $S_1$  and  $S_2$  and AoP for each reference frame. © The Authors. Published by SPIE under a Creative Commons Attribution 4.0 Unported License. Distribution or reproduction of this work in whole or in part requires full attribution of the original publication, including its DOI. [DOI: 10.1117/1.0E.58.8.082418]

Keywords: atmospheric polarization; angle of polarization reference plane; polarimetry; atmospheric optics.

Paper 181707SS received Nov. 29, 2018; accepted for publication Apr. 22, 2019; published online May 20, 2019.

#### 1 Introduction

Polarization is a property of light that is being increasingly recognized as a source of additional information for many remote sensing applications. In the atmosphere, the primary source of polarization is scattering by gas molecules; however, aerosols, 1-5 clouds, 6-8 and underlying surface reflectance<sup>9,10</sup> alter the observed sky polarization. To interpret polarization measurements or simulations correctly, it is important to understand how partially polarized skylight varies with environmental factors, <sup>1-10</sup> as well as with wavelength and solar position. <sup>10–12</sup> This is critical for military, environmental, and navigational applications. For example, military sensing and surveillance applications exploit scattered, reflected, or emitted polarization to detect objects on the ground, in the air, and in space because polarization provides an added dimension beyond intensity and color. <sup>13–16</sup> Environmental remote sensing applications are being developed that use ground-based, airborne, and spaceborne polarimeters to retrieve aerosol<sup>17-20</sup> and cloud properties, <sup>12,20-2</sup> which are important parameters needed in weather and climate models<sup>23–25</sup> and in optical communications.<sup>26–31</sup> Furthermore, inspired by insects and birds that use polarization for navigation, 32-37 polarization imagers are now being designed as navigational systems that use the angle of polarization (AoP) as a polarized light compass<sup>38–42</sup> for use when GPS is degraded or denied. In addition, all-sky polarimetry is now being used as a calibration source to determine polarization cross-talk properties of large telescopes.<sup>43</sup>

Polarized light can be described by the Stokes vector  $\vec{S}$ , containing the parameters  $S_0$ ,  $S_1$ ,  $S_2$ , and  $S_3$  (also referred to as I, Q, U, V).  $S_0$  represents the total irradiance (Wm<sup>-2</sup>),  $S_1$  represents the difference between 0 deg and 90 deg polarization,  $S_2$  represents the difference between 45 deg and 135 deg polarization, and  $S_3$  represents the difference

between right- and left-hand circular polarized light (in Earth's atmosphere for nearly all conditions, the amount of circularly polarized light is negligible<sup>10</sup>). The Stokes parameters can be used to derive the degree of linear polarization (DoLP) and the AoP. DoLP describes the fraction of intensity attributable to linearly polarized light and varies between 0 for random polarization and 1 for total polarization. AoP indicates the angle between the plane of polarization and a reference plane.

When aligned to a specific reference frame (RF), the Stokes parameters and derived AoP can provide unique information when analyzing sky polarization data for each application. Motivated by the rapidly broadening variety of applications that use or are affected by sky polarization, often by users who are not experts in sky polarization, this paper reviews the methods for converting between commonly used sky polarization RFs and for the first time shows a measured all-sky polarization image sequence from sunrise to sunset to illustrate how the sky polarization pattern varies spatially and temporally when visualized in the instrument, scattering, and solar principal planes. The methods presented by Schutgens et al. 44 and Li et al. 45 were used to align the Stokes parameters referenced in the instrument plane to the scattering and solar principal planes, respectively, for each pixel. To our knowledge, this paper is the first to show the same set of all-sky images of Stokes parameters and derived DoLP and AoP in each of these planes of reference. This paper is, therefore, a useful resource for readers who want a single source that not only outlines the math used to rotate between the polarimetric frames of reference, but also shows measurements during a wide range of solar geometries for all three RFs. In the balance of the paper, Sec. 2 describes the all-sky polarimeter used to obtain the images shown here, Sec. 3 defines the three different polarization reference planes and the methods used to convert the Stokes parameters and AoP between them, Sec. 4 shows all-sky Stokes, DoLP, and AoP images in the three different reference planes, and Sec. 5 provides conclusions.

<sup>\*</sup>Address all correspondence to Joseph A. Shaw, E-mail: joseph.shaw@montana.edu

#### 2 All-Sky Imaging Polarimeter

The all-sky polarization images shown in this paper were measured with the 450-nm channel of a multiwavelength, ground-based, all-sky imaging Stokes polarimeter. He Two liquid crystal variable retarders (LCVRs) were used to electronically vary the retardance of the imager so that a full Stokes image of the incident light was measured within a few tenths of a second. The polarimeter was calibrated using an external rotating polarizer and an integrating sphere viewed at numerous angles to fully capture the imager's system matrix over the entire fisheye field of view ( $\sim$ 160 deg) for each pixel. Maximum error for the linear Stokes parameters was estimated to be  $\pm 1.2\%$  with 100% linear input. This instrument has been used to characterize how skylight polarization changes with aerosols,  $^{4.5}$  clouds,  $^{6.7}$  and the underlying surface reflectance.

#### 3 Sky Polarization Reference Planes

The skylight DoLP has a distinct pattern that rotates through the sky in time, based on the position of the sun. A maximum band of polarization occurs ~90 deg from the sun, as shown in the all-sky images of Fig. 1 for morning (a), midday (b), and afternoon (c). These and all other all-sky images in this paper are displayed with north at the top and west at the right, as would be seen for an observer lying on the ground, looking up into the sky (this orientation is frequently used for upward-viewing all-sky imagers<sup>8,46–48</sup>). The direct sun view is blocked with a disk mounted on the moving sun occulter that stretches across the lower portion of these images. The DoLP is zero near the sun and in this image increases to a maximum value of ~60% in an arc located 90 deg from the sun. Although Rayleigh scattering theory predicts 100% polarization at a scattering angle of 90 deg, the actual maximum DoLP value is smaller because of multiple scattering from aerosols and the ground. 1-10 This pattern moves through the sky with the sun, with a magnitude that changes with environmental conditions and wavelength. 11,12 The DoLP pattern is, however, independent of the orientation of the polarizing elements used in the measurements. These particular measurements were recorded with the all-sky polarimeter during a solar eclipse field experiment<sup>49</sup> in Rexburg, Idaho (43.8295 °N, 111.8850 °W).

Unlike the DoLP, the AoP and the angle-dependent Stokes parameters,  $S_1$  and  $S_2$ , change with the reference

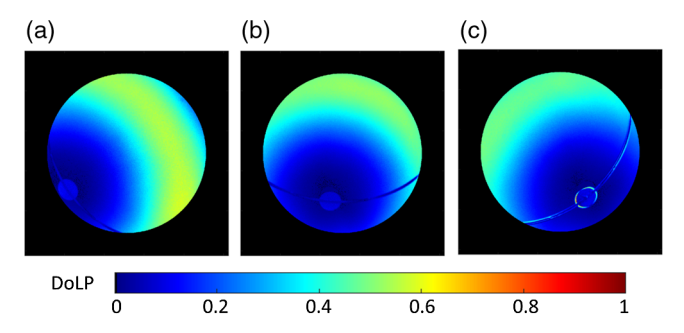


**Fig. 1** DoLP images with solar azimuth and zenith angles corresponding to, from left to right, 123 deg, 183 deg, 230 deg, and 45 deg, 32 deg, 42 deg, respectively. Measurements were recorded in Rexburg, Idaho, on 21 August 2017, at (a) 17:00:03, (b) 19:36:20, and (c) 21:34:06 UTC. The top of the image represents north and the right side of the image represents west.

plane. For each pixel, these angle-dependent parameters can be referenced to the instrument, scattering, and solar principal planes to be defined next, while the Stokes  $S_0$  and DoLP are independent of RF.

#### 3.1 Instrument Plane Reference

In the instrument plane of reference, the recorded angledependent Stokes parameters,  $S_1$  and  $S_2$ , and the derived AoP are referenced to the axis of the instrument's internal polarizer, with the AoP measured counterclockwise from the reference axis (for an observer looking towards the source). An example showing how the fixed-instrument AoP changes with solar position is in Fig. 2 (again, with the all-sky images oriented with north at the top and west to the right). In Fig. 2, all-sky AoP images are shown for three different solar positions: the left-hand image is for morning (sun in the southeast), the center image is for midday (sun to the south), and the right-hand image is for afternoon (sun in the southwest). Displaying these measurements with respect to the instrument plane causes the AoP patterns to change with solar position (these patterns would remain constant with solar position if they were shown relative to the continually evolving scattering plane, to be discussed next).

#### 3.2 Scattering Plane Reference

To compare measured AoP results with Rayleigh scattering theory, a transformation of the coordinate system is needed to align the reference plane to each pixel's unique scattering plane. The scattering plane, denoted by the gray plane S, O, and  $v_p$  in Fig. 3, contains the direction of incident sunlight and scattered light in the viewing direction for the observer position. Once rotated into the scattering plane, the AoP and angle-dependent Stokes parameters have a uniform distribution throughout the sky and this pattern rotates with the solar position, as observed in Fig. 4, where the AoP is ~90 deg for each pixel in the all-sky image. Note also in Fig. 4 that neutral points are observed near the sun and are represented by a 90 deg change in AoP. Neutral points, locations with zero polarization, arise from multiple scattering creating polarization oriented parallel to the scattering plane, which offsets the polarization oriented perpendicular to the scattering plane (which arises from first-order scattering). In Fig. 4, neutral points exist just below and just above the sun.

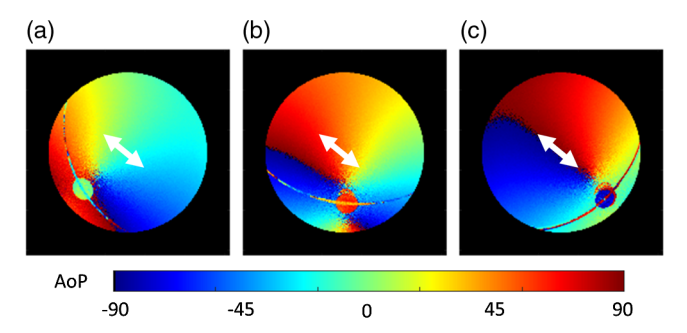


**Fig. 2** AoP images referenced to the instrument plane with solar azimuth and zenith angles corresponding to, from left to right, 123 deg, 183 deg, 230 deg, and 45 deg, 32 deg, 42 deg, respectively. Measurements were recorded in Rexburg, Idaho, on 21 August 2017, at (a) 17:00:03, (b) 19:36:20, and (c) 21:34:06 UTC (same as in Fig. 1). The AoP was referenced to the axis of the internal polarizer (white arrow) and measured counterclockwise. The top of the image represents north and the right side of the image represents west.

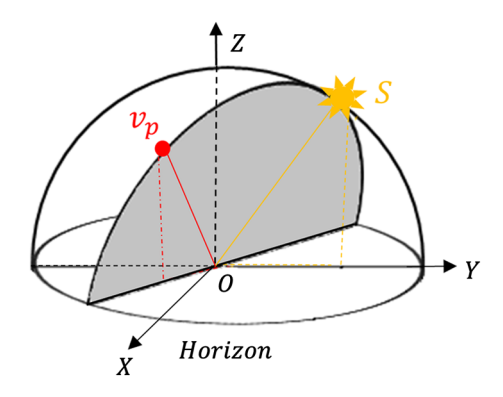


**Fig. 3** Scattering plane illustration. The solar scattering plane contains the directions of incident light and scattered light in the viewing direction of the observer denoted by the gray plane S, O, and  $v_D$ .

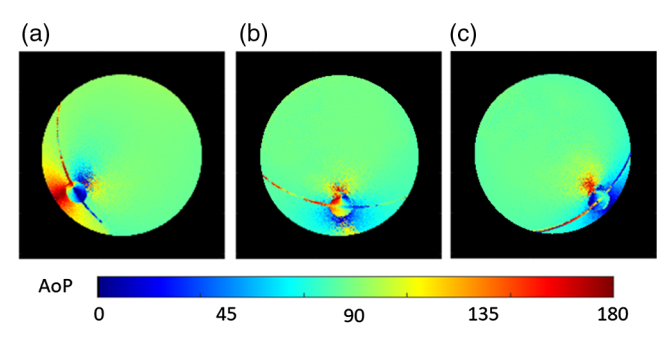


**Fig. 4** AoP images referenced to the scattering plane. Measurements were recorded in Rexburg, Idaho, on 21 August 2017, at (a) 17:00:03, (b) 19:36:20, and (c) 21:34:06 UTC (from the same images as in Figs. 1 and 2). The top of the image represents north and the right side of the image represents west.

#### 3.2.1 Instrument → Scattering plane calculation

The method presented by Schutgens et al.<sup>44</sup> was applied to transform the AoP measured in the instrument plane to an AoP referenced to the scattering plane at each pixel. Once the AoP was rotated, the normalized Stokes  $S_1$  and  $S_2$  parameters in the new RF could be calculated using Eqs. (1) and (2):

$$\left(\frac{S_1}{S_0}\right)_{RF} = \text{DoLP}_{\text{ins}} * \cos(2 * \text{AoP}_{RF}), \tag{1}$$

$$\left(\frac{S_2}{S_0}\right)_{RF} = \text{DoLP}_{\text{ins}} * \sin(2 * \text{AoP}_{RF}), \tag{2}$$

where DoLP<sub>ins</sub> represents the DoLP in the instrument plane of reference. The calculations in this method were based on the single-scattering Rayleigh model, in which the AoP is perpendicular to the scattering plane that contains the source, the scattered light from the viewing direction, and the observation point. In Fig. 5, the incident and scattered light is described by the zenith and azimuth angles,  $(\theta_i, \phi_i)$  and  $(\theta, \phi)$ , respectively. The azimuth angle for each view angle (pixel) of the polarimeter is referenced to north and is defined with respect to a right-hand coordinate reference, using the positive zenith direction as the axis of rotation. In practice, we related each pixel of the fisheye image to its corresponding zenith and azimuth angles by performing a spatial calibration.

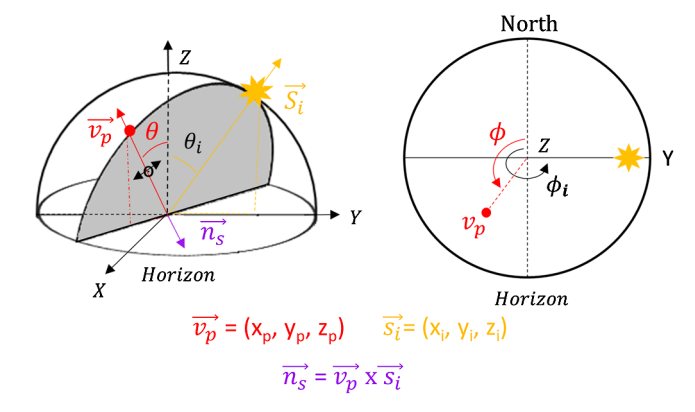


**Fig. 5** Solar scattering plane with reference notation. The solar scattering plane contains the directions of incident light  $(\vec{S_i})$  and scattered light  $(\vec{V_p})$  in the observer's viewing direction. The scattered light has a polarization vector orthogonal to the light ray. The scattering plane normal vector is  $\vec{n_s}$ .

Rotation of the AoP originally referenced to the instrument plane into a scattering-plane reference required calculation of the cross-product

$$\vec{n}_s = \vec{v}_p \times \vec{s}_i \tag{3}$$

of the incident light vector that points in the direction of the source  $(\vec{s_i})$  and the scattered light vector that points in the viewing directions

$$\vec{v_p} = (\cos \emptyset \sin \theta, \sin \emptyset \sin \theta, \cos \theta). \tag{4}$$

This defines the scattering plane unique to each pixel in the image. The AoP can be found using Eq. (5),

$$AoP_{sp} = \theta_{sp} = arc cosine \left( \frac{\vec{v_p} \cdot \vec{n_s}}{|\vec{v_p}||\vec{n_s}|} \right), \tag{5}$$

where  $\vec{v_p}$  is again the light entering the system and  $\vec{n_s}$  is the vector normal to the scattering plane. Figure 6 shows the angle between these two vectors.

#### 3.3 Solar Principal Plane Reference

AoP measurements are also commonly aligned to the solar principal plane. For this RF, the scattered light  $\vec{v_p}$  is referenced to the solar principal plane, which contains the incident light and local zenith, denoted by the gray plane S, O,

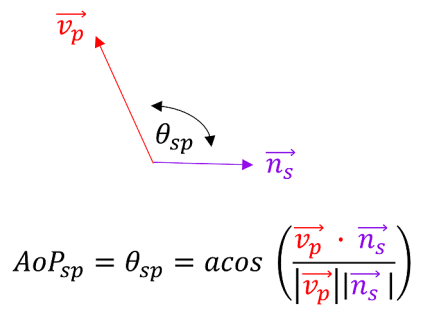


**Fig. 6** The angle between the light entering the system  $(\vec{v_p})$  and the vector normal to the scattering plane  $(\vec{n_s})$  is the AoP referenced to the scattering plane. This is found by taking the arc cosine of the dot product of the two vectors,  $\vec{v_p}$  and  $\vec{n_s}$ , as shown in Eq. (5).

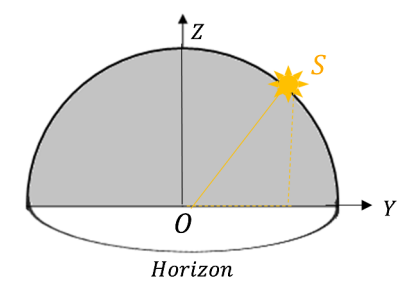


**Fig. 7** Solar principal plane illustration. The solar principal plane contains the incident light and local zenith denoted by the gray plane S, O, and Z.

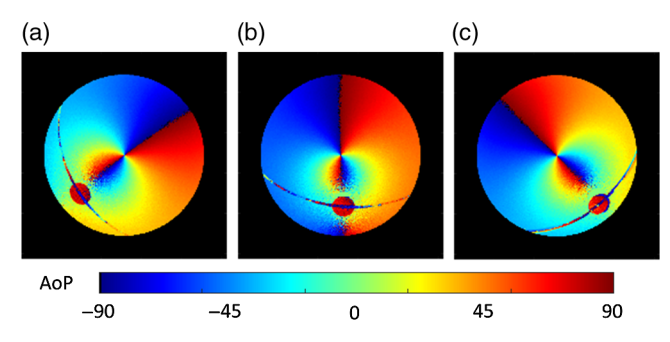


**Fig. 8** (a)–(c) AoP images referenced to the solar principal plane with solar azimuth and zenith angles corresponding to, from left to right, 123 deg, 183 deg, and 230 deg, and 45 deg, 32 deg, 42 deg, respectively (from the same images as in Figs. 1, 2, and 4). In this RF, the AoP is measured clockwise from the solar principal plane (matching the approach used in Ref. 48). The top of the image represents north and the right side of the image represents west.

and Z in Fig. 7. This results in each instrument-frame AoP value being aligned to the solar principal plane, which creates a common reference coordinate system for all pixels and a similar AoP pattern that rotates with the solar position, as shown in Fig. 8.

#### **3.3.1** Instrument → Solar principal plane calculation

The method presented by Li et al.<sup>45</sup> was used to transform the Stokes  $S_1$  and  $S_2$  parameters from the instrument plane to the solar principal plane by using a rotation Mueller matrix [Eq. (6)]. The AoP in the solar principal plane was then derived from the realigned Stokes parameters. The reference coordinate system was transformed by rotating each pixel from the instrument plane by a counterclockwise rotation angle  $\alpha$  (Fig. 9):

$$\begin{bmatrix} S_0 \\ S_1 \\ S_2 \\ S_3 \end{bmatrix}_{\text{principal-plane}} = L[\alpha] \cdot \begin{bmatrix} S_0 \\ S_1 \\ S_2 \\ S_3 \end{bmatrix}$$

$$= \begin{bmatrix} 1 & 0 & 0 & 0 \\ 0 & \cos(2\alpha) & \sin(2\alpha) & 0 \\ 0 & -\sin(2\alpha) & \cos(2\alpha) & 0 \\ 0 & 0 & 0 & 1 \end{bmatrix} \begin{bmatrix} S_0 \\ S_1 \\ S_2 \\ S_3 \end{bmatrix}_{\text{instrument}}.$$
(6)

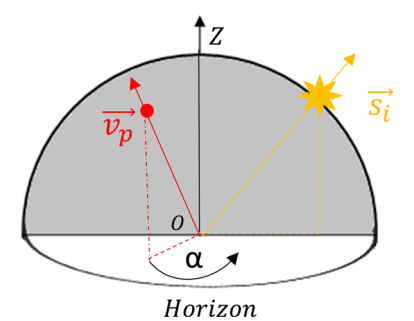


**Fig. 9** Reference coordinate system with the solar principal frame represented by the gray plane. The reference coordinate system can be transformed by rotating each Stokes pixel referenced in the instrument plane by a counterclockwise rotation angle  $\alpha$ , which represents the azimuth angle measured from the solar principal plane to the rotated pixel.

## 4 All-Sky Polarization Images in Each Plane of Reference

In Fig. 10, all-sky polarization Stokes  $S_1$ ,  $S_2$ , AoP, and DoLP images can be viewed, referenced to the instrument plane (left column), scattering plane (middle column), and solar principal plane (right column). The DoLP magnitude did not change in the different RFs (row 4 of Fig. 10); however,

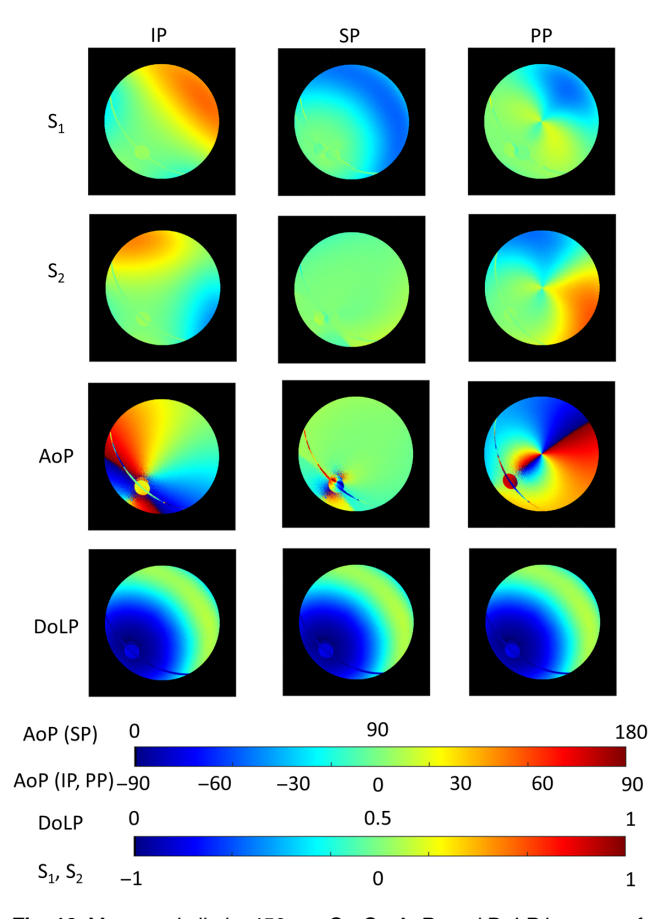


**Fig. 10** Measured all-sky 450 nm  $S_1$ ,  $S_2$ , AoP, and DoLP images referenced to the instrument plane (IP), scattering plane (SP), and solar principal plane (PP). The images were recorded with the LCVR all-sky polarimeter at 17:00:03 UTC on 21 August 2017, in Rexburg, Idaho. The solar azimuth angle and zenith angle were 123.1 deg and 45.0 deg, respectively. The top of the image represents north and the right side of the image represents west.

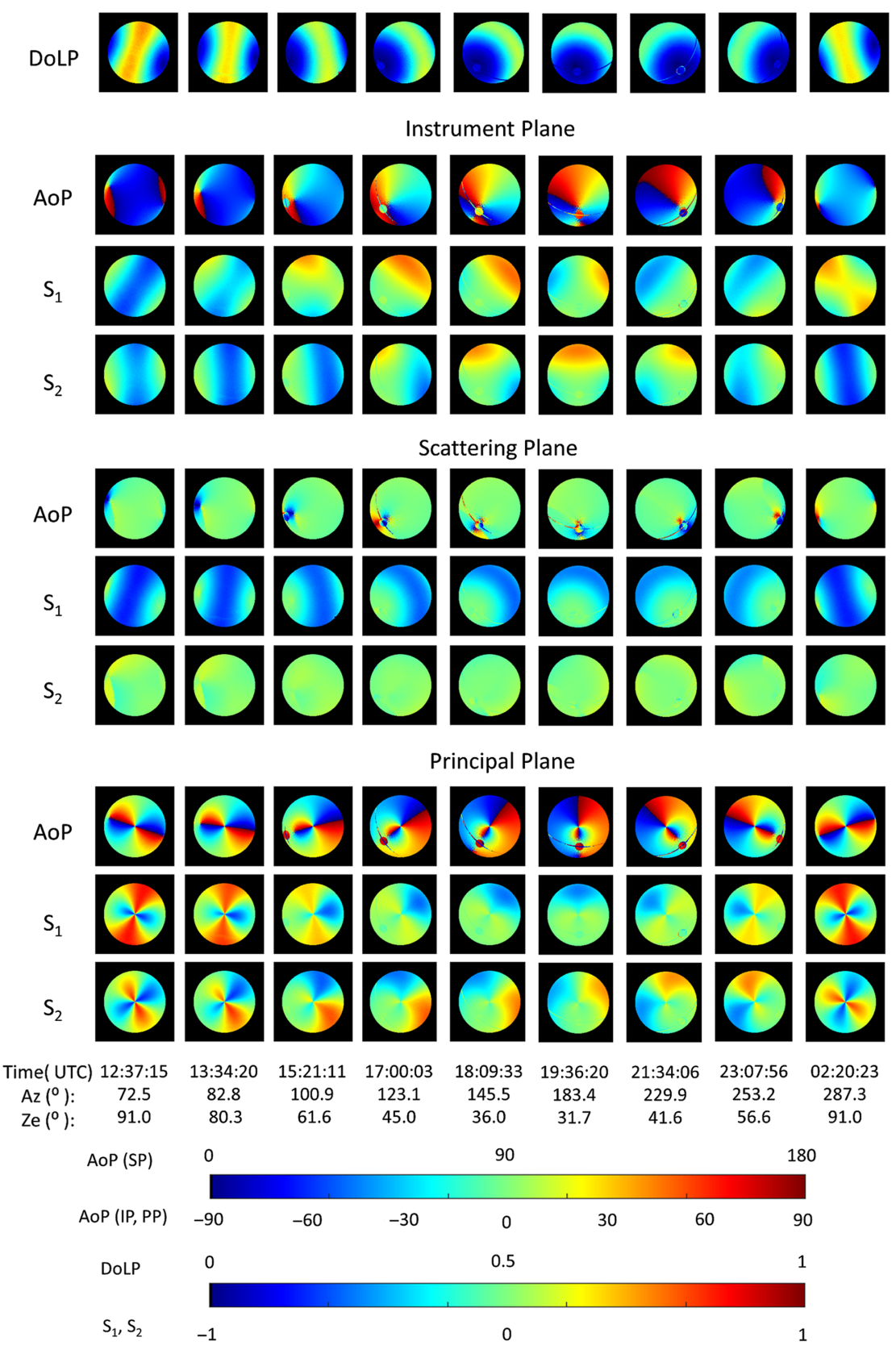


**Fig. 11** Time series of DoLP (independent of RF, row 1), AoP,  $S_1$ , and  $S_2$  images measured with the LCVR all-sky polarimeter (450 nm) referenced to the instrument plane (rows 2–4), scattering plane (rows 5–7), and solar principal plane (rows 8–10). The measurements were recorded in Rexburg, Idaho, on 21 August 2017. Each column represents a separate measurement with the corresponding time and solar azimuth and zenith angles positioned below the column. The top of the image represents north and the right side of the image represents west.

the  $S_1$ ,  $S_2$ , and AoP images exhibit significant changes with RF, as illustrated with the measured image sequence presented in Fig. 11. This sequence is for a clear sky observed throughout an entire day from pre-sunrise (left) to postsunset (right). The DoLP images (Fig. 11, row 1) show the band of maximum polarization moving through the sky from sunrise to sunset, always nominally 90 deg from the sun. Because the DoLP is independent of measurement RF, it is shown only once at the top of the image. However, as the solar geometry changed, the  $S_1, S_2$ , and AoP images referenced in the instrument, scattering, and solar principal planes also changed. For measurements referenced to the instrument plane (Fig. 11, rows 2–4), the  $S_1$ ,  $S_2$ , and AoP images varied based on the position of the sun with respect to the orientation of the imager's reference polarizer. Referencing the polarization angles in the scattering plane created uniform  $S_1, S_2$ , and AoP images (Fig. 11, rows 5–7) that rotated with the solar position. For single scattering, the clear-sky AoP is always perpendicular to the scattering plane, so in the scattering-plane reference, the AoP is  $\pm 90$  deg in all pixels except in the vicinity of neutral points. As the solar position changes, the AoP referenced to the solar principal plane (Fig. 11, rows 8–10) is  $\pm 90$  deg only in the solar principal plane that contains the sun and the zenith, and depends on the solar scattering geometry for all other pixels.

The  $S_1$  and  $S_2$  values, which are related to the AoP through AoP =  $\frac{1}{2} \tan^{-1}(\frac{S_2}{S_1})$ , vary with solar geometry and instrument orientation in the instrument RF. However, when referenced to the scattering plane,  $S_1$  creates a spatial pattern that is similar to the DoLP, in which the band of maximum DoLP is replaced by a band of maximum  $S_1$  magnitude. In the scattering-plane reference, all pixels have  $S_2 = 0$  except where numerical artifacts cause small discrepancies. When referenced to the solar principal plane, a bow-tie-shaped region of negative  $S_1$  runs along the principal plane, while a similar bow-tie region of positive  $S_1$  runs perpendicular to the principal plane (with both bow ties centered on the zenith). The principal-plane-referenced  $S_2$  pattern is similar but rotated by 45 deg in azimuth.

#### 5 Conclusions

The angle-dependent parameters for sky polarization measurements must be expressed relative to a known reference plane. In this paper, we described the process of converting from the default instrument reference plane to the more broadly used solar principal-plane and scattering-plane references and showed all-sky images of the angle-dependent Stokes parameters and derived AoP for direct comparison in these three RFs. When aligned to a specific reference plane, the angle-dependent Stokes parameters and derived AoP can provide unique information for analysis of sky polarization data for military, environmental, and navigational applications. The different RFs make unique features of the polarization pattern more or less apparent. This paper serves as a reference to the methods used to transform sky polarization into different references frames, but, most importantly, it is a resource for readers who wish to visualize and understand how sky polarization patterns vary throughout the day in the different RFs.

#### Acknowledgments

This material is based on research sponsored by the Air Force Research Laboratory, under agreement number FA9550-14-1-0140. The US Government is authorized to reproduce and distribute reprints for Governmental purposes notwithstanding any copyright notation thereon. The views and conclusions contained herein are those of the authors and should not be interpreted as necessarily representing the official policies or endorsements, either expressed or implied, of the Air Force Research Laboratory or the US Government.

#### References

- 1. D. R. Bates, "Rayleigh scattering by air," Planet. Space Sci. 32, 785–790 (1984).
- 2. E. Boesche et al., "Effect of aerosol microphysical properties on polarization of skylight: sensitivity study and measurements," Appl. Opt. 45, 8790–8805 (2006).
- 3. A. Kreuter, C. Emde, and M. Blumthaler, "Measuring the influence of aerosols and albedo on sky polarization," Atmos. Res. 98, 363-367,
- N. J. Pust et al., "Comparison of full-sky polarization and radiance observations to radiative transfer simulations which employ AERONET products," *Opt. Express* 19, 18602–18613 (2011).
   J. A. Shaw, N. J. Pust, and E. Forbes, "Effects of wildfire smoke on atmospheric polarization," *Proc. SPIE* 9099, 909907 (2014).
   L. M. Eshelman, M. J. Tauc, and J. A. Shaw, "All-sky polarization imaging of cloud thermodynamic phase," *Opt. Express* 27, 3528–3541 (2019).
- (2019).
- 7. N. J. Pust and J. A. Shaw, "Digital all-sky polarization imaging of partly cloudy skies," *Appl. Opt.* 47, H190–H198 (2008). 8. G. Horváth et al., "Ground-based full-sky imaging polarimetry of
- rapidly changing skies and its use for polarimetric cloud detection," *Appl. Opt.* **41**, 543–559 (2002).
- 9. A. R. Dahlberg, N. J. Pust, and J. A. Shaw, "Effects of surface reflectance on skylight polarization measurements at the Mauna Loa Observatory," Opt. Express 19, 16008–16021 (2011).
- 10. K. L. Coulson, Polarization and Intensity of Light in the Atmosphere,
- A. Deepak Publishing, Hampton, Virginia (1988).
  11. N. J. Pust and J. A. Shaw, "Wavelength dependence of the degree of polarization in cloud-free skies: simulations of real environments,"
- polarization in cloud-tree skies: simulations of real environments," Opt. Express 20(14), 15559–15568 (2012).
   L. M. Eshelman and J. A. Shaw, "The VIS-SWIR spectrum of skylight polarization," Appl. Opt. 57, 7974–7986 (2018).
   S. J. Tyo et al., "Review of passive imaging polarimetry for remote sensing applications," Appl. Opt. 45, 5453–5469 (2006).
   F. Goudail et al., "Target detection with a liquid-crystal-based passive Stokes polarimeter," Appl. Opt. 43, 274–282 (2004).
   D. A. Lavigne et al., "Target discrimination of man-made objects using passive polarimetric signatures acquired in the visible and infrared.

- passive polarimetric signatures acquired in the visible and infrared spectral bands," *Proc. SPIE* **8160**, 816007 (2011).
- 16. S. Lin et al., "Polarization enhanced visual surveillance techniques," in IEEE Int. Conf. Networking, Sens. and Control, Vol. 1, pp. 216-221
- 17. Z. Li et al., "Retrieval of aerosol optical and physical properties from ground-based spectral, multi-angular, and polarized sun-photometer measurements," *Remote Sens. Environ.* **101**(4), 519–533 (2006).

  18. J. Deuz'e et al., "Remote sensing of aerosols over land surfaces from
- POLDER-ADEOS-1 polarized measurements," J. Geophys. Res.: Atmos. **106**, 4913–4926 (2001).
- 19. G. van Harten et al., "Atmospheric aerosol characterization with a groundbased SPEX spectropolarimetric instrument," Atmos. Meas. Tech. 7, 4341-4351 (2014).
- G. van Harten et al., "Calibration and validation of Airborne Multiangle SpectroPolarimetric Imager (AirMSPI) polarization measurements," Appl. Opt. 57, 4499–4513 (2018).

  21. K. Knobelspiesse et al., "Cloud thermodynamic phase detection with
- polarimetrically sensitive passive sky radiometers," *Atmos. Meas. Tech.* **8**, 1537–1554 (2015).

  22. M. J. Tauc et al., "Cloud thermodynamic phase detection with a
- 3-channel shortwave infrared polarimeter," Proc. SPIE 10655, 1065500 (2018).
- 23. V. Ramanathan et al., "Cloud-radiative forcing and climate: results from the Earth radiation budget experiment," Science 243, 57-63 (1989).
- 24. O. Boucher et al., In Climate Change 2013: The Physical Science Basis. Contribution of Working Group I to the Fifth Assessment Report of the Intergovernmental Panel on Climate Change, Cambridge University Press, Cambridge/New York (2013).
- W. B. Rossow and R. A. Schiffer, "Advances in understanding clouds from ISCCP," *Bull. Am. Meteorol. Soc.* 80, 2261–2287 (1999).

- 26. A. Deepak, U. O. Farrukh, and A. Zardecki, "Significance of higherorder multiple scattering for laser beam propagation through hazes, fogs, and clouds," *Appl. Opt.* **21**(3), 439–447 (1982).

  S. Jaruwatanadilok, A. Ishimaru, and Y. Kuga, "Optical imaging
- through clouds and fog," IEEE Trans. Geosci. Rem. Sens. 41(8), 1834–1843 (2003).
- S. Arnon and N. S. Kopeika, "Adaptive optical transmitter and receiver for space communication through thin clouds," Appl. Opt. 36(9), 1987-1993 (1997).
- F. Courvoisier et al., "Ultraintense light filaments transmitted through clouds," *Appl. Phys. Lett.* 83(2), 213–215 (2003).
   S. Arnon, D. Sadot, and N. S. Kopeika, "Analysis of optical pulse dis-
- tortion through clouds for satellite to earth adaptive optical communi-
- cation," *J. Mod. Opt.* **41**(8), 1591–1605 (1994).

  31. S. Piazzolla and S. Slobin "Statistics of link blockage due to cloud cover
- for free-space optical communications using NCDC surface weather observation data," *Proc. SPIE* **4635**, 138–149 (2002).

  32. B. Greiner et al., "Anatomical and physiological evidence for polarisation vision in the nocturnal bee Megalopta genalis," *J. Comp. Physiol. A* 193, 591-600 (2007).
- 33. E. Warrant and M. Dacke, "Visual orientation and navigation in noctur-
- s. E. Warrain and M. Dacke, "visual orientation and navigation in nocturnal anthropods," *Brain Behav. Evol.* **75**, 156–173 (2010).
  s. F. Able, "Skylight polarization patterns and the orientation of migratory birds," *J. Exp. Biol.* **141**, 241–256 (1989).
  s. J. B. Phillips and F. R. Moore, "Calibration of the sun compass by sun-
- set polarized light patterns in a migratory bird," Behav. Ecol. Sociobiol. **31**, 189 (1992).
- 36. I. Pomozi, G. Horvath, and R. Wehner, "How the clear-sky angle of polarization pattern continues underneath clouds: full-sky measurements and implications for animal orientation," J. Exp. Biol. 204, 2933–2942 (2001).
- 37. S. B. Karman, S. Z. M. Diah, and I. C. Gebeshuber, "Bio-inspired polarized skylight-based navigation sensor: a review," Sensors 12(11),

- polarized skylight-based havigation sensor, a review, sensors 12(11), 14232–14261 (2012).
   D. Lambrinos et al., "An autonomous agent navigating with a polarized light compass," Adapt. Behav. 6, 131–161 (1997).
   T. Ma et al., "An evaluation of skylight polarization patterns for navigation," Sensors 15, 5895–5913 (2015).
   H. Zhao et al., "Polarization patterns under different sky conditions and a navigation method based on the symmetry of the AOP map of already in the symmetry of th
- and a haygaton method based on the symmetry of the AO1 map of skylight," *Opt. Express* **26**, 28589–28603 (2018).

  41. T. Aycock et al., "Passive optical sensing of atmospheric polarization for GPS denied operations," *Proc. SPIE* **9838**, 98380Y (2016).

- 42. A. Barta et al., "Polarization transition between sunlit and moonlit skies with possible implications for animal orientation and Viking navigation: anomalous celestial twilight polarization at partial moon," Appl. Opt. **53**, 5193–5204 (2014).
- D. M. Harrington, J. R. Kuhn, and A. L. Ariste, "Daytime sky polarization calibration limitations," *Proc. SPIE* 9912, 99126S (2016).
   N. A. J. Schutgens et al., "On the relationship between stokes param-
- eters q and u of atmospheric ultraviolet/visible/near-infrared radiation," Geophys. Res.: Atmos. 109(D9), D09205 (2004).
- 45. L. Li et al., "A method to calculate Stokes parameters and angle of polarization of skylight from polarized CIMEL sun/sky radiometers," Quant. Spectrosc. Radiat. Transfer 149, 334-346 (2014).
- 46. N. J. Pust and J. A. Shaw, "Dual-field imaging polarimeter using liquid crystal variable retarders," *Appl. Opt.* 45, 5470–5478 (2006).
  47. J. Gál et al., "Polarization patterns of the summer sky and its neutral
- points measured by full-sky imaging polarimetry in Finnish Lapland north of the Arctic Circle," *Proc. R. Soc. Lond. A* **457**, 1385–1399 (2.001)
- 48. G. Horvath, I. Pomozi, and J. Gal, "Neutral points of skylight polarization observed during the total eclipse on 11 August 1999," Appl. Opt.
- **42**(3), 465–475 (2003).

  49. L. M. Eshelman et al., "All-sky polarization measurements of the total solar eclipse on 21 August 2017," *Proc. SPIE* **10655**, 106550L (2018).

Laura M. Eshelman completed her PhD in electrical engineering at Montana State University in 2018. She received her BA degree in physics from Gustavus Adolphus College in 2013 and her MS degree in electrical engineering from Montana State University in 2015. She is a member of SPIE and her work focuses on studying atmospheric polarization using all-sky imaging systems.

Joseph A. Shaw received his PhD and MS degrees in optical sciences from the University of Arizona, MS degree in electrical engineering from the University of Utah, and BS degree in electrical engineering from the University of Alaska. He is the director of the Optical Technology Center and professor of optics and photonics and electrical engineering at Montana State University, Bozeman. His research is developing optical remote sensing systems. He is a fellow of OSA and SPIE and is the 2019 recipient of the G. G. Stokes Award from SPIE.